NEMA NU 2-2001 Performance Measurements of an LYSO-Based PET/CT System in 2D and 3D Acquisition Modes

Brad J. Kemp[1], Chang Kim[2], John J. Williams[2], Alexander Ganin[2], and Val J. Lowe[1]

[1]*Department of Radiology, Mayo Clinic, Rochester, Minnesota; and* [2]*Functional Imaging, GE Healthcare, Waukesha, Wisconsin*

The National Electrical Manufacturers Association (NEMA) NU 2-2001 performance measurements were conducted on the Discovery RX, a whole-body PET/CT system under development by GE Healthcare. The PET scanner uses $4.2 \times 6.3 \times 30$ mm lutetium yttrium orthosilicate (LYSO) crystals grouped in 9×6 blocks. There are 24 rings with 630 crystals per ring and the ring diameter is 88.6 cm. The transaxial and axial fields of view are 70.0 and 15.7 cm, respectively. The scanner has retractable septa and can operate in both 2-dimensional (2D) and 3-dimensional (3D) modes. 2D acquisitions use ring differences of ± 4 for direct and ± 5 for cross slices; 3D acquisitions use a ring difference of 23. The coincident window width is 6.5 ns and the energy window is 425–650 keV. Other than the detectors, the system uses the same hardware and software as a Discovery ST. The CT scanner is a 16-slice LightSpeed; the performance characteristics of the CT component are not included herein. **Methods:** Performance measurements of sensitivity, spatial resolution, image quality, scatter fraction and counting rate performance, and image quality were obtained using NEMA methodology. **Results:** The system sensitivity in 2D and 3D was measured as 1.7 cps/kBq and 7.3 cps/kBq, respectively. The transaxial resolution for 2D (3D) was 5.1 mm full width at half maximum (FWHM) (5.0 mm) at 1 cm from gantry center and the radial and tangential resolutions were 5.9 mm (5.9 mm) and 5.1 mm (5.2 mm) at 10 cm, respectively. The axial resolution for 2D (3D) was 4.8 mm FWHM (5.8 mm) and 6.3 mm (6.5 mm) at 1 cm and 10 cm from gantry center, respectively. The scatter fraction was 13.1% and 31.8% in 2D and 3D. The peak noise equivalent count rate (NECR) was 155 kcps at 92.1 kBq/mL in 2D and 117.7 kcps at 21.7 kBq/mL in 3D for a noise-free estimation of randoms. The contrast of the 22, 17, 13, and 10 mm hot spheres in the image quality phantom in 2D (3D) were 74.6% (72.4%), 56.7% (59.5%), 46.2% (44.6%), and 17.9% (18.0%), respectively. **Conclusion:** The Discovery RX is a scanner that possesses high NECR, low scatter fraction, and good spatial resolution characteristics.

Key Words: National Electrical Manufacturers Association; PET; whole-body imaging; lutetium yttrium orthosilicate

J Nucl Med 2006; 47:1960–1967

Received Apr. 12, 2006; revision accepted Sep. 5, 2006.

For correspondence or reprints contact: Brad J. Kemp, PhD, Department of Radiology, Mayo Clinic, 200 First St. SW, Rochester, MN 55905.

E-mail: kemp.brad@mayo.edu

Commercial whole-body PET scanners have used various scintillators from sodium iodide (NaI(Tl)) (*1*): bismuth germinate (BGO) (*2–4*), lutetium oxyorthosilicate (LSO) (*5,6*), and gadolinium oxyorthosilicate (GSO) (*7*). Depending on the scanner requirements, these scintillators all have desirable properties, such as high effective atomic number, density and light yield, fast decay time, and favorable physical (rugged, nonhygroscopic) characteristics (*8,9*). To be sure, the selection of a scintillator depends on the performance specifications of the tomograph, with cost of manufacturing and the availability of raw materials also being important considerations. Moreover, the performance of the scanner depends not only on the scintillator but also on the scanner design as a whole, which includes the collection of light, photomultiplier tube performance, spatial encoding within the block detector, and electronic architecture and design (*10*).

Another cerium-doped oxyorthosilicate scintillator is lutetium yttrium orthosilicate (LYSO). LYSO possess excellent characteristics for detecting 511-keV photons in PET: The effective atomic number is 65; the density is 7.1 g/cm^3, and the attenuation coefficient is 0.83 cm^{-1} at 511 keV; the scintillation decay time is 42 ns and it has a light yield that is similar to that of LSO (*11–14*). It should be mentioned that the values of these properties depend on the relative yttrium content.

The performance characteristics of a new whole-body PET/CT scanner that uses LYSO scintillators are presented. This system, called the Discovery RX, has been developed by GE Healthcare. The design of the PET system is based on the Discovery ST scanner (*4,15*); it uses the same hardware and software as a Discovery ST except that it uses LYSO as the scintillator. The imaging characteristics of the Discovery RX were measured using the National Electrical Manufacturers Association (NEMA) performance standards NU 2-2001 (*16*).

MATERIALS AND METHODS

PET System Design

The PET scanner uses LYSO crystals of dimensions $4.2 \times 6.3 \times 30$ mm in the tangential, axial, and radial directions respectively. The yttrium content of the LYSO crystals is approximately 6%,

expressed as a molar percentage of yttrium content relative to lutetium. The LYSO crystals are arranged into 9×6 blocks, and each block is coupled to a 4-anode, square photomultiplier tube. Eight blocks are grouped into a module in a 2 by 4 arrangement in the tangential and axial directions. There are 35 modules in the scanner, and, as a result, there are 24 rings with 630 LYSO crystals per ring.

The ring diameter is 88.6 cm and the transaxial and axial fields of view are 70.0 and 15.7 cm, respectively. The system produces 47 images with a slice thickness of 3.27 mm from a single frame. The patient port is also 70 cm in diameter. The scanner has retractable tungsten septa (54 mm length, 0.8 mm thick) and can operate in both 2-dimensional (2D) and 3-dimensional (3D) modes. The 2D acquisitions use ring differences of ±4 for direct and ±5 for cross slices; the 3D acquisitions use a ring difference of 23. The coincidence window width is 6.5 ns and the energy window is 425−650 keV for both 2D and 3D acquisitions. The mean energy resolution measured for all crystals is 14%. System calibration and daily quality control is facilitated through the use of a 60 MBq ^{68}Ge rotating rod source. The CT scanner is a 16-slice LightSpeed; the performance characteristics of the CT component are not included herein.

The LYSO scintillator contains the radionuclide ^{176}Lu, which decays by β-emission and a subsequent cascade of γ- and x-rays. The resultant intrinsic true (from the detection of a β-emission in one detector and a single γ-ray in a second detector) and random coincidences that are detected are indistinguishable from the true and random coincidences from the extrinsic radiation (*6,17*). For the Discovery RX, the intrinsic radiation from ^{176}Lu results in a background coincidence counting rate (with no object within the scanner, measured from a 10 h scan) of 1,100 cps and 2,700 cps in 2D and 3D, respectively, of which 1 and 8 cps are true coincidence counting rates for 2D and 3D. Hence, the true coincidence counting rate from the intrinsic radiation can be considered negligible. However, the intrinsic counting rate means that the conditions required for NEMA NU 2-2001 cannot be met for all performance measurements (*6,17*). For example, the counting rate and scatter fraction (SF) measurement requires a randoms-to-true coincident event ratio (RTR) of <0.01, which is not possible for this scanner as the minimum RTR is 0.10 in 2D and 0.19 in 3D. Therefore, for the counting rate and sensitivity metrics, both the prompt and delayed coincident events were measured to correct for the intrinsic random events. Any deviation from the current NEMA NU 2-2001 methodology will be outlined.

Phantoms

As specified by NEMA, three phantoms were used to conduct the performance measurements: a scatter phantom, sensitivity phantom, and image quality phantom. The scatter phantom is a circular polyethylene cylinder with an outside diameter of 203 mm and a length of 700 mm. A 6.4 mm hole is located off-axis at a radial distance of 45 mm and runs parallel to the central axis of the cylinder. Plastic tubing (800 mm length, 3.2 mm diameter) representing a line source is inserted into this hole. The sensitivity phantom consists of five nested metal sleeves of known thickness and 700 mm length. Activity is placed in a plastic tube and threaded through the inner sleeve. The image quality phantom consists of the IEC (International Electrotechnical Commission) body phantom and a lung insert. Within the body phantom are six fillable spheres; the two largest spheres are cold, whereas the four small spheres are filled with activity. The spheres are positioned in a 114 mm circle such that their centers are located in the same transaxial plane. The lung insert has a density of 0.30 g/cm^3 and is located in the center of the phantom.

SF and Counting Rate Measurements

The SF and counting rate measurements were performed using the NEMA scatter phantom (Computerized Imaging Reference Systems Inc.) with separate acquisitions for the 2D and 3D measurements. The line source was filled with 7.2 GBq of ^{18}F for the 2D acquisition and 1.0 GBq of ^{18}F for the 3D acquisition. The phantom was positioned such that the line source was centered within the axial field of view (FOV) and located nearest the bed. A total of 88 static scans (72 scans of 10 min duration with no interscan delay followed by 16 scans of 25 min with a 5 min interscan delay) were acquired. For each of these acquisitions, both prompt and delayed coincident events sinograms were acquired. The counting rate loss was <1% in late frames.

Single-slice rebinning was applied to collapse the oblique 3D data (both the prompts and delayed events) into a single sinogram for each slice. The prompts and delayed-event sinograms were masked to a 240 mm FOV, and the prompts sinogram was shifted such that the maximum activity in each projection was located in the central pixel. The total events ($C_{TOT,i,j}$) and random events ($C_{r,i,j}$) were calculated as the integral of counts within slice i of the masked prompts and delayed sinograms of acquisition j. The random and scatter events for slice i of acquisition j ($C_{r+s,i,j}$) were computed as the sum of the counts outside a central 40 mm strip in the prompts sinogram plus a fraction of counts within this 40 mm strip, as stipulated by NEMA. It should be noted that $C_{r+s,i,j}$ includes the intrinsic coincident events.

The true event rate for slice i of acquisition j was defined as:

$$R_{t,i,j} = \frac{(C_{TOT,i,j} - C_{r+s,i,j})}{T_{acq,j}},$$

and the system true event rate $R_{t,j}$ was the sum of $R_{t,i,j}$ over all slices i. The random event rate for slice i of acquisition j is defined as:

$$R_{r,i,j} = \frac{C_{r,i,j}}{T_{acq,j}},$$

and the system random event rate $R_{r,j}$ was the sum of $R_{r,i,j}$ over all slices i. The scatter event rate for slice i of acquisition j was defined as:

$$R_{s,i,j} = \frac{C_{r+s,i,j} - C_{r,i,j}}{T_{acq,j}},$$

and the system scatter event rate $R_{s,j}$ was the sum of $R_{s,i,j}$ over all slices. The SF for slice i of acquisition j was calculated as:

$$SF_{i,j} = \frac{C_{r+s,i,j} - C_{r,i,j}}{C_{TOT,i,j} - C_{r,i,j}},$$

and the system SF was computed as:

$$SF_j = \frac{\sum_i C_{r+s,i,j} - \sum_i C_{r,i,j}}{\sum_i C_{TOT,i,j} - \sum_i C_{r,i,j}}.$$

The effective activity concentration in the phantom, a_{eff}, was calculated as the activity in the line source divided by 22 kg. The

characteristic extrinsic activity threshold (denoted as a_{ref}), above which the counting rate from extrinsic radiation is greater than that from the intrinsic radiation, was computed for the 2D and 3D acquisitions (*17*). The SF was computed using the average of three measurements taken near a_{ref}.

The noise equivalent count rate (NECR) for slice i for acquisition j was defined as:

$$R_{NEC,i,j} = \frac{R_{t,i,j}^2}{R_{TOT,i,j} + kR_{r,i,j}},$$

where k = 0 for noiseless estimate of random events (denoted as NECR 1R) and k = 1 for direct random event subtraction (denoted as NECR 2R). The system noise equivalent count rate $R_{NEC,j}$ was computed as the sum of $R_{NEC,i,j}$ over all slices i. The maximum system true event rate $R_{t,j}$ and maximum system noise equivalent count rate $R_{NEC,j}$ and the effective activity concentrations at these maximums were reported.

Corrections for Count Losses and Randoms

The 2D and 3D sinograms acquired in the counting rate measurements were used to measure the accuracy of the corrections for dead-time losses and random events. Both 2D and 3D sinograms were reconstructed using filtered backprojection (FBP) into a 128 × 128 matrix with a FOV of 180 mm. Fourier rebinning (FORE) was applied to the 3D sinograms before FBP. Corrections for dead time, randoms, and normalization were applied; no corrections for attenuation and scatter were applied.

From the reconstructed images, the trues rate $R_{ROI,i,j}$ in the 180 mm FOV was computed for each slice i and each acquisition j. The extrapolated counting rate $R_{EXT,i,j}$ was computed by scaling the effective activity concentration at each acquisition j by the ratio of $R_{ROI,i,j}$ to a_{eff} for the three acquisitions with activity $\sim a_{ref}$. The relative counting rate error was computed as the bias of $R_{ROI,i,j}$ to $R_{EXT,i,j}$, expressed as a percentage. The maximum, minimum, and mean relative errors across all slices were calculated for each acquisition; the maximum absolute value of the bias was determined for those acquisitions with activity values at or below the activity at peak R_{NEC}.

Sensitivity

The sensitivity of the scanner was measured for the 2D and 3D acquisition modes. The line source of the NEMA sensitivity phantom (Data Spectrum) was filled with 16 MBq of ^{18}F and threaded through the inner aluminum sleeve. Successive measurements were acquired with up to five aluminum sleeves surrounding the line source for the phantom positioned in the center of transaxial FOV and at a distance of 100 mm from the scanner axis. 2D and 3D prompt and delayed-event sinograms were acquired for each sleeve configuration and at each location. The acquisition duration was 2 min for the 2D acquisitions (i.e., the acquisitions with the least counts); the minimum number of true coincident events in a slice was >18 kilocounts.

Single-slice rebinning was applied to the 3D prompts and delayed sinograms to assign each oblique line of response (LOR) to the slice where the LOR crosses the scanner axis. The total counts in each slice i of sleeve acquisition j of the prompts ($C_{TOT,i,j}$) and delays ($C_{r,i,j}$) sinograms were calculated. The true event rate was defined as:

$$R_{t,i,j} = \frac{(C_{TOT,i,j} - C_{r,i,j})}{T_{acq,j}},$$

and the system true event rate $R_{t,j}$ was the sum of $R_{t,i,j}$ over all slices i. The true event rates for each acquisition were corrected for activity decay. The natural logarithm of the true counting rate for each sleeve was plotted as a function of sleeve thickness and a linear equation was fit to the data. The counting rate without attenuation (i.e., sleeve thickness of zero) is represented by the intercept of this equation, and the total system sensitivity is the counting rate without attenuation divided by the activity in the line source. The sensitivity as a function of axial position was also generated using data acquired for the smallest tube at the center of the transaxial FOV.

Spatial Resolution

Spatial resolution measurements were performed with point sources made by placing ^{18}F in capillary tubes. The extent of the activity in the tubes was <1 mm in the transaxial and axial directions. The point sources were placed at locations, in centimeters, of (0, 1), (0, 10), and (10, 0) in the transaxial plane. In the axial plane, the point sources were placed at the center of the FOV and at one quarter of the extent of the axial FOV from the center. The duration of each 2D and 3D acquisition was 60 s.

Both 2D and 3D data were reconstructed with FBP with a ramp filter into a 256 × 256 matrix and a 250 mm FOV. FORE was applied to the 3D sinograms before FBP. Profiles of width ~ times the full width at half maximum ([FWHM] measured orthogonal to the direction of measurement) were generated through the peak of the reconstructed point source. The FWHM and full width at tenth maximum (FWTM) of the profiles were calculated using linear interpolation between adjacent pixels. The radial, tangential, and axial resolutions are reported.

Image Quality

The NEMA image quality phantom (PTW–New York) was used to simulate a whole-body acquisition. The four smaller spheres were filled with a 4:1 activity concentration relative to the background, with an activity concentration of 5.2 kBq/mL in the background. The plastic tubing of the scatter phantom was filled with 115 MBq, and the phantom was abutted to the image quality phantom to simulate activity outside the FOV. The image quality phantom was placed on the table such that the spheres were centered in the axial FOV. Note that with this phantom positioning there are some slices that do not contain the phantom or the lung insert.

NEMA NU 2-2001 methodology, which was devised before the introduction of PET/CT scanners, requires the simulation of a 100 cm emission and transmission scan in 60 min. However, with the transmission acquisition being supplanted by the CT acquisition most of this acquisition time is, by definition, devoted to the emission acquisition. This is not a realistic clinical acquisition but was kept as such to comply with NEMA methodology. The 2D acquisitions simulated a 3 slice overlap that resulted in an axial step of 144 mm and a frame duration of 8.5 min. Similarly, the 3D acquisition simulated a 7 slice overlap with a 131 mm axial step and subsequent frame duration of 7.8 min. Three 2D and 3D acquisitions were acquired in succession (2D acquisition 1, 3D acquisition 1, 2D acquisition 2, 3D acquisition 2, and so forth)

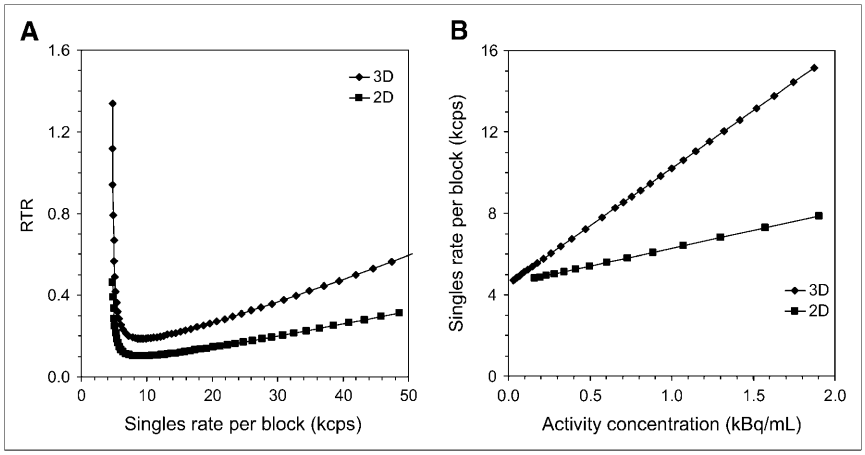

FIGURE 1. (A) RTR as function of average singles rate in a block detector for 2D and 3D acquisitions. Measurements were acquired during counting rate performance test. (B) Average singles rate per block as function of effective activity concentration. Graph shows that intrinsic radiation causes the singles rate of 4.5 kcps for an external activity concentration of zero.

with the acquisition duration adjusted for the physical decay. On average, the 3D sinograms contained 5.3 times more true coincident events than the 2D acquisitions (8.2×10^8 vs. 1.6×10^7 events).

The 2D sinograms were reconstructed with ordered-subsets expectation maximization ([OSEM] 3 iterations and 21 subsets), and the 3D sinograms were reconstructed with a fully 3D OSEM (3 iterations and 35 subsets) algorithm (*18*). For all reconstructions, a Gaussian postprocessing filter of 5 mm FWHM was applied. Both 2D and 3D data were reconstructed into a 500 mm FOV with a pixel size of 3.91 mm and slice thickness of 3.27 mm. The CT images were used for attenuation correction. For scatter correction, the technique of Bergstrom et al. (*19*) was used for the 2D acquisition and a model-based technique was used for the 3D acquisition (*20*). For correction of randoms coincidences, single-event counting rates (*21*) were used.

The count density in the spheres was determined by drawing regions of interest (ROIs) of diameter equal to the inner diameter of each sphere on the transaxial image through the center of the spheres. The CT images were used to assist in region placement. The background count density was obtained from ROIs drawn in the central slice and slices located ±10 mm and ±20 mm from this slice (12 ROIs per slice, 60 ROIs total). The contrast and background variabilities were calculated and expressed as a percentage for each sphere and averaged for the three acquisitions. The residual error in the lung was computed for each slice. An average error, computed across the 31 slices that contain the lung insert, was also calculated.

RESULTS

SF and Counting Rate Measurements

The RTR as a function of the singles rate per block is shown in Figure 1A for the 2D and 3D acquisitions. For the 3D acquisition it is apparent that the RTR never attains the 0.01 value as required by NEMA: The minimum RTR is 0.10 and 0.19 for the 2D and 3D acquisitions, respectively. The singles rate per block is plotted as a function of the effective activity concentration in the line source in Figure 1B. A linear regression was fit to these data, and the intercept—the singles rate for an activity concentration of zero—represents the singles rate due to the intrinsic radiation of the LYSO crystals, s_{int}. For the 2D acquisition, s_{int} was 4.5 kcps and a_{ref} was 2.6 kBq/mL or 57.2 MBq in the line source. For the 3D acquisition, s_{int} was 4.5 kcps and a_{ref} was 0.81 kBq/mL or 17.8 MBq in the line source.

The true and random counting rates are plotted as a function of the effective activity concentration in Figure 2. For the 2D acquisition (Fig. 2A), the maximum true

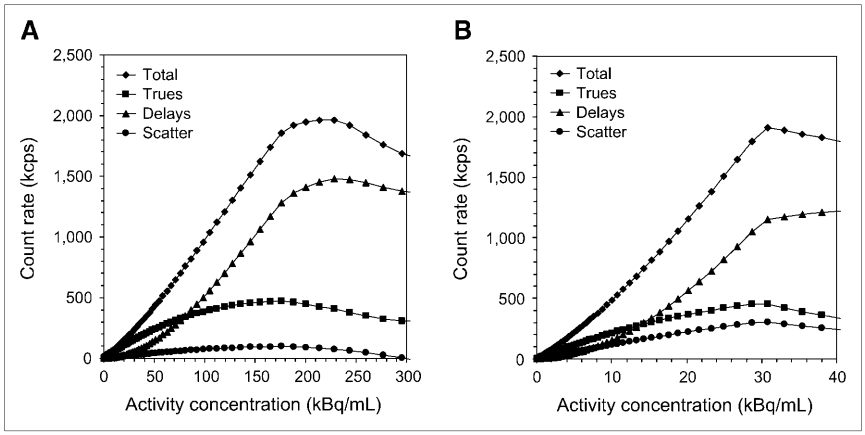

FIGURE 2. Counting rate performance for system operating in 2D (A) and 3D (B) modes.

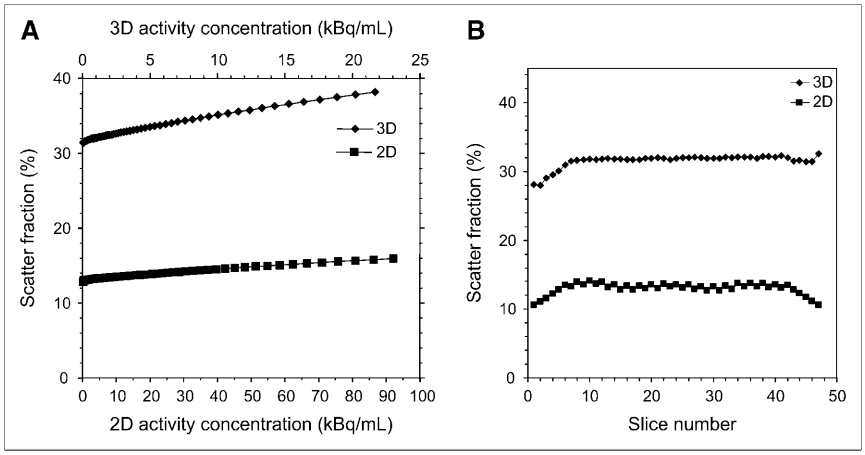

FIGURE 3. (A) 2D and 3D SFs of system as function of effective activity concentration, plotted up to activity at peak NECR. Curves have different *x*-axes to show increase in SF over similar singles rates. (B) SF of system as function of slice number in 2D and 3D acquisition modes.

counting rate was 473.2 kcps at an effective activity concentration of 176.0 kBq/mL. For the 3D acquisition (Fig. 2B), the maximum true counting rate was 453.6 kcps at an effective activity concentration of 30.8 kBq/mL.

The system SF was 13.1% for the 2D acquisition and 31.8% for the 3D acquisition. In addition, the system SF at peak NECR was 16.0% and 38.2% for the 2D and 3D acquisitions, respectively. The 2D and 3D SFs are plotted as a function of their respective effective activity concentration in Figure 3A. The SF increases as the effective activity increases, more so for the 3D acquisition. This effect, which needs further investigation, may be attributed to the higher singles rate causing pulse pileup effects. The SF as a function of slice is shown in Figure 3B.

The NECR curves are plotted as a function of the effective activity in Figure 4. For the 2D acquisition and a noiseless randoms estimate, the maximum NECR was 155.0 kcps at an effective activity concentration of 92.1 kBq/mL. The maximum NECR for delayed-event subtraction of randoms was 105.7 at 71.0 kBq/mL (Fig. 4A). For the 3D acquisition and a noiseless randoms estimate, the maximum NECR was 117.7 kcps at an effective activity concentration of 21.7 kBq/mL. The maximum NECR for delayed-event subtraction of randoms was 79.6 at 17.6 kBq/mL (Fig. 4B). Both the 2D and 3D NECR curves are broad and encompass a large range of effective activity concentrations.

Counting Rate Accuracy

The maximum, minimum, and mean relative counting rate errors for the 2D and 3D acquisitions are plotted in Figure 5. Shown on the plots are the effective activity concentrations at the peak NECR. For the 2D and 3D acquisitions, the absolute value of the maximum relative counting rate error is 3.0% and 5.0%, respectively, which occur at the effective activity concentration of the peak NECR (92.1 kBq/mL for 2D and 27.1 kBq/mL for 3D). The absolute value for the mean relative counting rate error is 0.8% and 4.5% for the 2D and 3D acquisitions, respectively, at this activity concentration.

Sensitivity

The system sensitivity for radial positions R0 and R10 were 1.66 cps/kBq and 1.70 cps/kBq, respectively, in 2D and 7.30 and 7.54 cps/kBq in 3D. The axial sensitivity

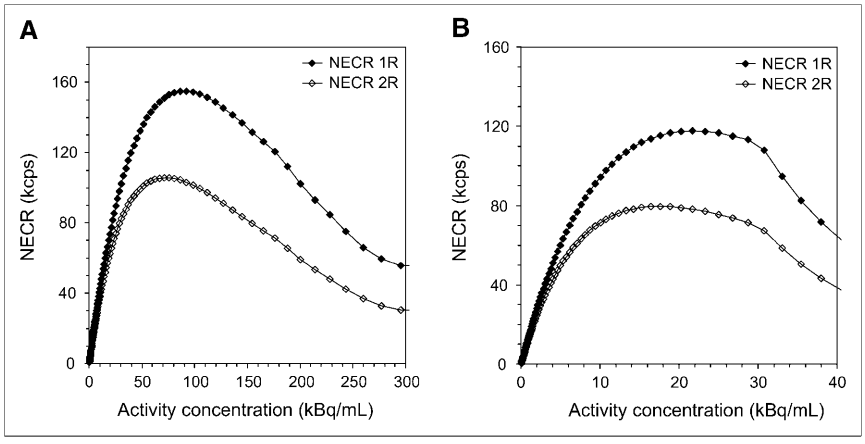

FIGURE 4. Noise equivalent count rate curves for scanner operating in 2D (A) and 3D (B) modes. NECR 1R denotes computation using a noiseless estimate of randoms events, whereas NECR 2R denotes computation using delayed-event subtraction.

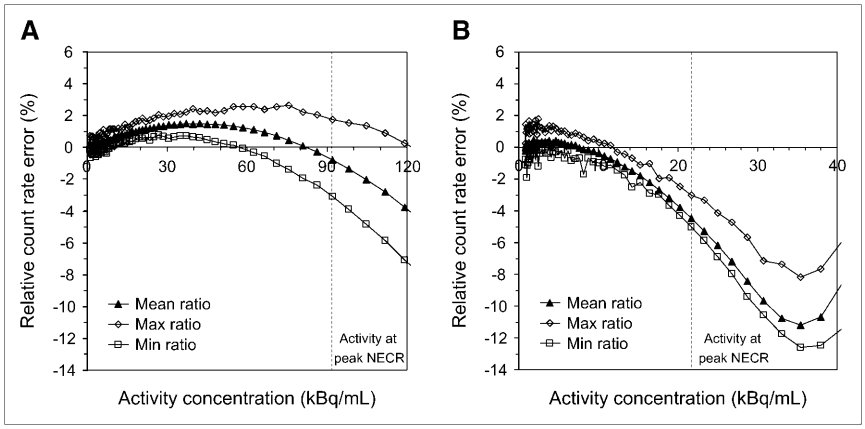

FIGURE 5. Plots of relative counting error as function of effective activity concentration for 2D (A) and 3D (B) modes. Plotted are maximum, minimum, and mean relative counting errors across all slices. Dashed line indicates activity concentration at maximum NECR.

profile for the 2D and 3D acquisitions of the inner sleeve at the scanner center are shown in Figure 6.

Resolution

The transaxial and axial resolutions for the 2D and 3D acquisition modes are listed in Table 1. At a distance of 1 cm from the central axis of the scanner, the transaxial FWHM (and FWTM) of the 2D acquisition is comparable to the transaxial FWHM (and FWTM) of the 3D acquisition; a similar trend is present for the transaxial resolution at 10 cm from the central axis. As expected, there is some radial elongation of the 2D and 3D resolutions at a 10 cm distance from the central axis.

Image Quality

All spheres were visible in the reconstructed images of the image quality phantom. Furthermore, the background region did not exhibit any streak artifacts. The results of the image quality experiment are listed in Table 2. The contrasts for the spheres were comparable for the 2D and 3D acquisitions, with the exception of the 28 mm cold sphere. There is less variability in hot lesion contrast with the 3D acquisition. Also, the 3D images have better background variability.

The average value for the residual error in the lung for the 2D OSEM reconstruction was 20.6% ± 1.5% and for the fully 3D OSEM reconstruction the residual error was 19.0% ± 0.9%. The estimated SF for the 2D acquisitions was 18%, whereas the model-based scatter correction estimated the SF as 24% for the 3D acquisitions.

DISCUSSION

We have presented the NEMA NU2-2001 performance measurements of the Discovery RX PET/CT scanner under development by GE Healthcare. The scanner is based on the Discovery ST PET scanner but uses LYSO as the scintillator. As expected, the switch to LYSO from BGO has an effect on the system's performance. LYSO has a scintillation decay time of 42 ns; this fast decay time leads to a reduction in dead time and it enables improved timing resolution and a narrower coincidence timing window, which, in turn, reduces the number of random events. This reduction in the random coincidence rate is manifested in the high NECR. The scanner also has excellent counting rate capability. In 2D, the Discovery RX has a peak NECR of 155.0 at 92.1 kBq/mL, which is greater than the peak NECR of 90.2 kcps at 52.5 kBq/mL for the Discovery ST (*4*). Similarly, in 3D, the Discovery RX has a peak NECR

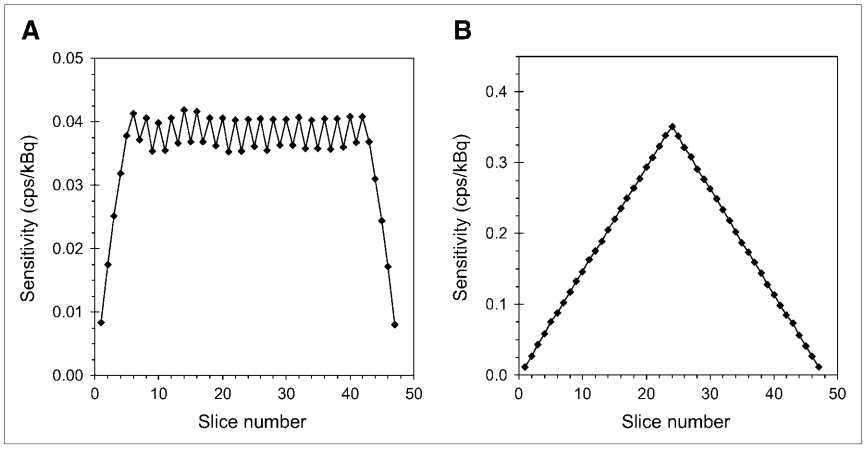

FIGURE 6. Axial sensitivity profile measured for 2D (A) and 3D (B) acquisition modes. Shown are profiles for the line source at center of the gantry.

TABLE 1
Spatial Resolution Measurements for 2D and 3D Acquisition Modes

Distance = 1 cm				
	Transaxial		Axial	
Mode	FWHM (mm)	FWTM (mm)	FWHM (mm)	FWTM (mm)
2D	5.1	9.7	4.8	10.6
3D	5.0	9.7	5.8	11.5

Distance = 10 cm						
	Transaxial: radial		Transaxial: tangential		Axial	
Mode	FWHM (mm)	FWTM (mm)	FWHM (mm)	FWTM (mm)	FWHM (mm)	FWTM (mm)
2D	5.9	11.6	5.1	10.2	6.3	12.9
3D	5.9	11.4	5.2	10.3	6.5	12.7

of 117.7 at 21.7 kBq/mL, which is greater than the peak NECR of 67.8 kcps at 12.0 kBq/mL for the Discovery ST (*4*). This counting rate capability is important for 3D studies or high-counting-rate studies in 2D but may not be realized in clinical 2D whole-body studies. It should also be noted that the peak NECR for patient studies occurs at a lower activity level than that for the NEMA performance measurement (*22*).

LYSO also has a higher light yield than BGO, which permits the use of smaller crystals within a block detector and the subsequent separation of the individual crystals in the position map. This results in improved spatial resolution. A high light yield also results in good energy resolution; the energy discrimination window can be narrowed (i.e., the lower level discriminator raised) and the SF thereby reduced. The SFs of 13.1% for 2D and 32.1% for 3D acquisitions are lower than the respective SFs of 19.1% and 45.1% for the Discovery ST (*4*). This improved performance can be attributed to the increased light yield and subsequent narrower energy window of the Discovery RX. In the SF measurement, there was an increase in the SF as the effective activity increases, especially for the 3D acquisition. This increase in SF as a function of activity may have an effect on clinical studies acquired in 3D, depending on the relative activities in the patient and the performance of the scatter correction.

The system sensitivity in 2D and 3D is lower than the sensitivity of the Discovery ST (1.7 vs. 1.9 cps/kBq in 2D and 7.2 vs. 9.1 cps/kBq in 3D for Discovery RX and ST, respectively). This difference can be attributed to the wider energy window used on the Discovery ST (375–650 keV) and the BGO scintillator. In 3D, the axial sensitivity profile is peaked in the center of the axial FOV. This has implications in clinical imaging, as a large slice overlap will need to be used if the fluctuations in sensitivity as a function of slice are to be reduced.

The Discovery RX has good transaxial resolution that remains relatively stable as the source is moved from the center of the gantry. The system resolution is not isotropic because of the crystal dimensions. The transaxial resolution for both the 2D and 3D acquisition modes are very similar.

CONCLUSION

The NEMA NU2-2001 performance measurements show that the Discovery RX possesses high NECR, low SF, and good spatial resolution characteristics.

TABLE 2
Image Quality Measurements for 2D and 3D Acquisition Modes

		Sphere diameter (mm)					
Measurement	Mode	10	13	17	22	28	37
Contrast (%)							
	2D	17.9 ± 3.6	46.2 ± 4.6	56.7 ± 5.3	74.6 ± 5.1	77.1 ± 2.6	78.5 ± 2.4
	3D	18.0 ± 1.2	44.6 ± 1.8	59.5 ± 1.8	72.4 ± 3.4	65.0 ± 1.1	73.6 ± 0.9
Background variability (%)							
	2D	10.8 ± 1.1	9.1 ± 1.5	7.3 ± 0.9	5.8 ± 0.8	4.8 ± 0.4	3.6 ± 0.2
	3D	6.0 ± 0.7	5.0 ± 0.6	4.3 ± 0.5	3.7 ± 0.3	3.2 ± 0.2	2.7 ± 0.2

Values are expressed as mean ± SD from three acquisitions and measurements.

REFERENCES

1. Adam LE, Karp JS, Daube-Witherspoon ME, Smith RJ. Performance of a whole-body PET scanner using curve-plate NaI(Tl) detectors. *J Nucl Med.* 2001;12:1821–1830.
2. DeGrado TR, Turkington TG, Williams JJ, Stearns CW, Hoffman JM, Coleman RE. Performance characteristics of a whole-body PET scanner. *J Nucl Med.* 1994; 35:1398–1406.
3. Brix G, Zaers J, Adam LE, et al. Performance evaluation of a whole-body PET scanner using the NEMA protocol. *J Nucl Med.* 1997;38:1614–1623.
4. Mawlawi O, Podoloff DA, Kohlmyer S, et al. Performance characteristics of a newly developed PET/CT scanner using NEMA standards in 2D and 3D modes. *J Nucl Med.* 2004;45:1734–1742.
5. Melcher CL, Schweitzer JS. Cerium-doped lutetium oxyorthosilicate: a fast, efficient new scintillator. *IEEE Trans Nucl Sci.* 1992;39:502–505.
6. Erdi YE, Nehmeh SA, Mulnix T, Humm JL, Watson CC. PET performance measurements for an LSO-based combined PET/CT scanner using the National Electrical Manufacturers Association NU 2-2001 standard. *J Nucl Med.* 2004;45:813–821.
7. Surti S, Karp JS. Imaging characteristics of a 3-dimensional GSO whole-body PET camera. *J Nucl Med.* 2004;45:1040–1049.
8. Humm JL, Rosenfeld A, Del Guerra A. From PET detectors to PET scanners. *Eur J Nucl Med Mol Imaging.* 2003;30:1574–1597.
9. Surti S, Karp JS, Kinahan PE. PET instrumentation. *Radiol Clin North Am.* 2004;42:1003–1016.
10. Karp JS. Against: Is LSO the future of PET? *Eur J Nucl Med Mol Imaging.* 2002; 29:1525–1528.
11. Cooke DW, McClellan KJ, Bennet BL, Roper JM, Whittaker MT, Muenchausen RE. Crystal growth and optical characterization of cerium-doped $Lu_{1.8}Y_{0.2}SiO_5$. *J Appl Phys.* [serial on CD-ROM]. 2000;88:7360–7762.
12. Kimble T, Chou M, Chai BHT. Scintillation properties of LYSO crystals. In: Metzler SD, ed. *2002 IEEE Nuclear Science Symposium and Medical Imaging Conference Record* [book on CD-ROM]. Norfolk, VA: Institute of Electrical and Electronics Engineers; 2002.
13. Chai BHT, Ji Y, inventors; University of Central Florida and Crystal Photonics, Inc., assignees. Lutetium yttrium orthosilicate single crystal scintillation detector. US patent 6 624 420. September 23, 2003.
14. Chen J, Zhang L, Zhu RY. Large size LYSO crystals for future high energy experiments. *IEEE Trans Nucl Sci.* 2005;52:3133–3140.
15. Bettinardi V, Danna M, Savi A, et al. Performance evaluation of the new whole-body PET/CT scanner: Discovery ST. *Eur J Nucl Med Mol Imaging.* 2004;31: 867–881.
16. National Electrical Manufacturers Association. *Performance Measurements of Positron Emission Tomographs.* NEMA Standards Publication NU 2-2001. Rosslyn, VA: National Electrical Manufacturers Association; 2001.
17. Watson CC, Casey ME, Eriksson L, Mulnix T, Adams D, Bendriem B. NEMA NU 2 performance tests for scanners with intrinsic radioactivity. *J Nucl Med.* 2004;45:822–826.
18. Iatrou M, Manjeshwar RM, Ross SG, et al. Implementation and analysis of a 3D iterative reconstruction algorithm for the Discovery ST PET/CT scanners [abstract]. *J Nucl Med.* 2005;46(suppl):56P.
19. Bergstrom M, Eriksson L, Bohm C, Blomqvist G, Litton J. Correction for scattered radiation in a ring detector positron camera by integral transformation of the projections. *J Comput Assist Tomogr.* 1983;7:42–50.
20. Wollenweber SD. Parameterization of a model-based 3-D PET scatter correction. *IEEE Trans Nucl Sci.* [serial on CD-ROM]. 2002;49:722–727.
21. Stearns CW, McDaniel DL, Kohlmyer SG, Arul PR, Geiser BP, Shanmugan V. Random coincidence estimation from single event rates on the Discovery ST PET/CT scanner. In: Metzler SD, ed. *2003 IEEE Nuclear Science Symposium and Medical Imaging Conference Record* [book on CD-ROM]. Portland, OR: Institute of Electrical and Electronics Engineers; 2003.
22. Watson CC, Casey ME, Bendriem B, et al. Optimizing injected dose in clinical PET by accurately modeling the counting-rate response functions specific to individual patient scans. *J Nucl Med.* 2005;46:1825–1834.